

Two-Stage Heterogeneous Graph Neural Network for RIS-Aided Physical-Layer Security

Zihan Song, Yang Lu, *Senior Member, IEEE*, Wei Chen, *Senior Member, IEEE*, Bo Ai, *Fellow, IEEE*, Zhiguo Ding, *Fellow, IEEE*, and Arumugam Nallanathan, *Fellow, IEEE*

Abstract—This paper investigates physical-layer security (PLS) enabled by graph neural networks (GNNs). We propose a two-stage heterogeneous GNN (HGNN) to maximize the secrecy energy efficiency (SEE) of a reconfigurable intelligent surface (RIS)-assisted multi-input-single-output (MISO) system that serves multiple legitimate users (LUs) and eavesdroppers (Eves). The first stage formulates the system as a bipartite graph involving three types of nodes—RIS reflecting elements, LUs, and Eves—with the goal of generating the RIS phase shift matrix. The second stage models the system as a fully connected graph with two types of nodes (LUs and Eves), aiming to produce beamforming and artificial noise (AN) vectors. Both stages adopt an HGNN integrated with a multi-head attention mechanism, and the second stage incorporates two output methods: beam-direct and model-based approaches. The two-stage HGNN is trained in an unsupervised manner and designed to scale with the number of RIS reflecting elements, LUs, and Eves. Numerical results demonstrate that the proposed two-stage HGNN outperforms state-of-the-art GNNs in RIS-aided PLS scenarios. Compared with convex optimization algorithms, it reduces the average running time by three orders of magnitude with a performance loss of less than 4%. Additionally, the scalability of the two-stage HGNN is validated through extensive simulations.

Index Terms—PLS, two-stage, HGNN, RIS.

I. INTRODUCTION

A. Background

RIS has been widely regarded as a key wireless coverage enabler for next-generation mobile communication systems [1]. Specifically, RIS can intelligently adjust the phase of incident electromagnetic waves without additional radio frequency chains, thus effectively improving wireless channel quality, extending coverage, and mitigating signal interference [2]. Its passive operation enables energy-efficient deployment, which aligns well with the requirements of green communications. The channel reconfigurability of RIS can enlarge the channel diversity among receivers, which can be leveraged to enhance PLS [3]. As demonstrated in [4], RIS-aided PLS can significantly improve the system SEE and secrecy sum rate

(SSR) even when there are no direct communication links, and the performance gain increases with the number of reflecting elements. Despite the advantages of RIS, efficiently optimizing RIS-assisted communication systems is non-trivial due to the deeply coupled BS-related and RIS-related parameters.

Existing optimization approaches for RIS can be categorized into three categories: 1) convex optimization (CVXopt)-based approach, 2) deep reinforcement learning (DRL)-based approach, and 3) learn-to-optimize approach. For example, the authors in [5], [6] and [7] investigated multi-user MISO systems assisted by RIS, employing CVXopt-based approaches to maximize the system SEE and sum rate, respectively. However, as reviewed in [8], most existing CVXopt-based methods mainly rely on alternating optimization (AO) or block coordinate descent (BCD) to tackle the deeply coupled variables, leading to high computational overhead and separate optimization losses. In contrast, DRL-based approaches have emerged as a promising joint-optimization solver for RIS-assisted systems. They have been validated to enable energy-efficient designs in RIS-assisted MISO [9], simultaneous wireless information and power transfer [10], and unmanned aerial vehicle mobile edge computing systems [11]. Nevertheless, DRL-based approaches learn from interactions in partially controllable wireless environments, thus suffering from limited generalization capability.

This paper focuses on the data-driven learn-to-optimize approach, which has been widely adopted as an efficient optimization solver for various wireless systems [12]. Specifically, existing studies have adopted multi-layer perceptrons (MLPs) [13], [14] and convolutional neural network (CNNs) [15], [16], respectively, to realize joint optimization for RIS-assisted systems. However, MLPs and CNNs are inherently limited by their fixed input and output dimensions, thus failing to provide satisfactory generalization performance in dynamic RIS-assisted systems. By contrast, GNNs can effectively overcome the limitation [17], [18]. As analyzed in [19], GNNs are well matched to the topology of wireless networks, thereby not only outperforming other models but also achieving strong adaptability to wireless dynamics. For example, GNNs have been shown to enable real-time, near-optimal and scalable inference for MISO systems, aiming to maximize the sum rate (SR) [20], energy efficiency (EE) [21] and SEE [22], respectively. Compared with non-RIS and non-PLS systems, RIS-aided PLS involves complicated heterogeneity among distinct entities, such as the BS, RIS, LUs, and Eves. Therefore, it is of great importance to align the deep learning (DL) model with both the system and the task. Existing works handle

Zihan Song and Yang Lu are with the School of Computer and Information Technology, Beijing Jiaotong University, Beijing 100044, China (e-mail: 23120405@bjtu.edu.cn, yanglu@bjtu.edu.cn).

Wei Chen and Bo Ai are with the School of Electronics and Information Engineering, Beijing Jiaotong University, Beijing 100044, China (e-mail: weich@bjtu.edu.cn, boai@bjtu.edu.cn).

Zhiguo Ding is with the School of Electrical and Electronic Engineering (EEE), Nanyang Technological University, Singapore 639798 (Zhiguo.ding@ntu.edu.sg).

Arumugam Nallanathan is with the School of Electronic Engineering and Computer Science, Queen Mary University of London, London and also with the Department of Electronic Engineering, Kyung Hee University, Yongin-si, Gyeonggi-do 17104, South Korea (e-mail: a.nallanathan@qmul.ac.uk).

the ‘‘heterogeneity’’ via two perspectives, i.e., framework and neural architecture. For the framework, the authors in [23], [24] developed a multi-stage GNN to sequentially generate the phase shift matrix and beamforming vectors. This framework inherits the algorithmic structure of conventional CVXopt-based approaches and enhances the model’s interpretability. For the neural architecture, the authors in [25]–[28] exploited HGNNs to capture the heterogeneity within RIS-assisted systems. These HGNNs exhibit superior scalability with respect to the system entities.

B. Contribution

Existing works have demonstrated that the model’s expressive capability can be enhanced from the perspectives of both framework and neural architecture. However, no existing work has yet integrated the advantages of these two aspects. To fill this gap, this paper proposes to utilize the two-stage framework and HGNNs for RIS-aided physical-layer security, which involves heterogeneous system entities (i.e., BS, RIS, LUs, and Eves) as well as dual-functional services. The contributions of this paper are summarized as follows.

- We consider a typical RIS-aided PLS system, in which a multi-antenna BS serves multiple LUs in the presence of Eves via both direct and cascaded links. The transmitted signals consist of both information-bearing signals for LUs and AN to disrupt Eves. We formulate an SEE maximization problem by jointly optimizing the beamforming and AN vectors, as well as the RIS phase shift matrix.
- We propose a two-stage HGNN to solve the formulated problem. Specifically, the first stage models the considered system as a bipartite graph and employs both edge-based and edge-free graph attention operators to map channel state information (CSI) to the phase shift matrix. The second stage models the system as a fully-connected graph with heterogeneous node types and adopts an edge-free graph attention operator and a semantic attention mechanism to map augmented effective CSI to the beamforming and AN vectors. The outputs of both stages are fed into an unsupervised loss function for end-to-end joint training.
- Analysis results are presented to validate that the proposed two-stage HGNN is scalable with respect to the number of RIS reflecting elements, LUs, and Eves. Numerical results are provided to corroborate the analytical findings. Furthermore, the superiority of the proposed two-stage HGNN is demonstrated through comparisons with the state-of-the-art GNNs. Additionally, ablation experiments are conducted to validate the effectiveness of the key components of the proposed model.

The rest of this paper is organized as follows. Section II reviews emerging AI-based RIS-aided wireless communication technologies. Section III introduces the system model and problem formulation. Section IV presents two heterogeneous graph representation methods for the system. Section V details the proposed two-stage HGNN, followed by a scalability analysis. Section VI presents numerical results and evaluations. Section VII concludes the paper.

Notation: The following mathematical notations and symbols are used throughout this paper. Bold lowercase letters (e.g., \mathbf{a}) denote column vectors, and bold uppercase letters (e.g., \mathbf{A}) denote matrices or higher-dimensional tensors. The set of real numbers is denoted by \mathbb{R} , and the set of $n \times m$ real matrices by $\mathbb{R}^{n \times m}$. Similarly, \mathbb{C}^n and $\mathbb{C}^{n \times m}$ denote the sets of n -dimensional complex column vectors and $n \times m$ complex matrices, respectively. For a complex number a , $|a|$ denotes its modulus, and $\Re(a)$ and $\Im(a)$ denote its real and imaginary parts, respectively. For a vector \mathbf{a} , $\|\mathbf{a}\|$ denotes its Euclidean norm. For a matrix \mathbf{A} , \mathbf{A}^T , \mathbf{A}^H , $\|\mathbf{A}\|$, and $\text{Trace}(\mathbf{A})$ represent its transpose, conjugate transpose, Frobenius norm, and trace (i.e., the sum of its diagonal elements), respectively. The notation $\mathbf{a}[i]$ denotes the i -th entry of vector \mathbf{a} ; $\mathbf{A}[i, j]$ denotes the element in the i -th row and j -th column of matrix \mathbf{A} ; and $\mathbf{A}[i, :]$ denotes the entire i -th row of \mathbf{A} . The operator $\text{Concat}(\cdot)$ denotes the concatenation of its inputs. The operator $\text{LeakyReLU}(\cdot)$ denotes the leaky rectified linear unit (ReLU) with a small negative slope for negative inputs.

II. RELATED WORKS

This section summarizes the related works on GNN-enabled RIS-assisted systems. To clearly highlight the novelty of this paper, we compare the proposed two-stage HGNN and existing GNN-based models in Table I.

A. GNN-Enabled RIS Transmission

Various GNNs have been leveraged to jointly optimize RIS-assisted systems. The authors in [23] modeled an RIS-assisted MISO system as a homogeneous graph and proposed a two-stage framework to solve a sum-rate maximization problem, where the first stage employed a graph attention network (GAT) to predict the phase shift matrix and the second stage utilized an MLP to generate beamforming vectors. The authors in [24] considered an RIS-assisted downlink pinching-antenna system, with the objective of optimizing both the sum rate (SR) and energy efficiency (EE). They proposed a three-stage GNN, where each stage modeled the system as a fully connected graph and adopted either a graph convolutional network (GCN) [29] or a GAT [30] to derive the transmit parameters.

In addition to the homogeneous graph, the heterogeneous graphs may be more suitable for RIS-assisted systems and enable the problem to be solved within a single-stage framework. The authors in [25] formulated an RIS-assisted MISO mmWave system into a heterogeneous graph with an RIS node and multiple user nodes, and proposed a modified GAT to map angular cascaded channels to beamforming vectors and reflection coefficients for sum-rate maximization. Besides, they adopted transfer learning in the model to adapt to variations in user counts. The authors in [26] formulated a sum-rate maximization problem for a system utilizing collaboration of an RIS and a relay, which includes two phases, i.e., BS-RIS-user phase and relay-RIS-user phase. Regarding the first phase, they modeled the system as a fully-connected heterogeneous graph with one RIS node and multiple user nodes, and adopted an HGNN to yield phase shift matrix

TABLE I
COMPARISON WITH EXISTING WORKS ON GNN-ENABLED RIS-ASSISTED SYSTEMS.

Ref.	Architecture	Objective	Multi-Stage	Heterogeneous	Residual	Attention	Generalization		
							LU	RIS	Eve
[23]	GAT+MLP	SR	✓	×	×	✓	×	×	—
[24]	GAT+GCN	SR/EE	✓	×	✓	✓	✓	✓	—
[25]	GCN+GAT	SR	×	✓	×	✓	×	×	—
[26]	HGNN	SR	×	✓	✓	×	✓	×	—
[27]	HGNN	EE	×	✓	✓	×	✓	×	—
[28]	HGNN	WSR	×	✓	✓	×	×	✓	—
[31]	HGNN	Max-Min	×	✓	×	×	✓	✓	—
[32]	HGNN	SR	×	✓	×	×	✓	✓	—
[33]	GNN	SSR	×	✓	✓	×	✓	×	×
[34]	CO-GNN	SSR	×	✓	×	✓	✓	×	✓
Our work	HGNN	SSE	✓	✓	✓	✓	✓	✓	✓

and beamforming vectors via different message aggregation methods. The authors in [27] considered an RIS-assisted MISO system covering both single-cell and cell-free scenarios and formulated an EE maximization problem. The system was represented as a heterogeneous graph with one RIS node and multiple user nodes, which was fed into a GNN with two distinct feature initialization strategies to jointly optimize and the phase shift matrices and beamforming vectors. The authors in [28] considered a multi-RIS-assisted system and formulated a sum-rate maximization problem. The system is represented by a fully-connected heterogeneous graph with a BS node, multiple RIS nodes and user nodes, and fed into an HGNN to jointly obtain the phase shift matrix, beamforming vectors and the RIS association matrix.

However, since all reflecting elements are represented by a single RIS node, the models in [25]–[28] are not scalable with respect to the number of reflecting elements. The authors in [31] considered an RIS-assisted cell-free system under imperfect CSI assumption and formulated a max-min uplink rate maximization problem. The system is represented by a heterogeneous graph comprising access point nodes, RIS reflecting element nodes, and user nodes. They proposed an advanced HGNN to jointly solve the problem. The authors in [32] considered a simultaneous transmitting and reflecting (STAR)-RIS-assisted MISO system and formulated a sum-rate maximization problem. They modeled the system using a bipartite graph and solved the problem with a beamforming HGNN based on a heterogeneous graph message-passing protocol, with guaranteed permutation equivariance and scalability.

B. GNN-Enabled RIS-Aided PLS

There are a limited number of works focusing on GNN-enabled RIS-aided PLS. The authors in [33] presented an RIS-assisted integrated sensing and communication (ISAC) system as a heterogeneous graph, which models LUs and an Eve as receiver nodes, and the RIS as an additional node. They utilized an HGNN to maximize the minimum secrecy rate. The authors in [34] considered an RIS-assisted non-orthogonal multiple access (NOMA) system encompassing

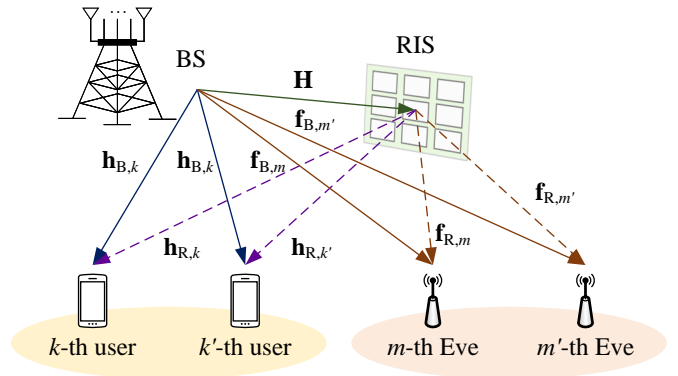


Fig. 1. An RIS-aided MISO PLS system, where a BS serves multiple LUs in the presence of multiple Eves.

downlink, uplink, and eavesdropping links. They modeled the system as a heterogeneous graph involving a BS node, a RIS node, and multiple LU nodes and Eve nodes. They proposed a combinatorial optimization GNN (CO-GNN) to maximize sum secrecy rate. However, the models proposed in [33] and [34] rely on a single-stage framework and lack scalability with respect to the number of reflecting elements.

From the related works, we derive the following observations for designing GNN-enabled RIS-assisted systems: 1) both the multi-stage framework and heterogeneous graph representation can enhance the model's expressive power; 2) sophisticated graph modeling enables strong scalability. Furthermore, the design of GNN architecture should be well aligned with the adopted framework and graph representation, which is crucial to the model performance. Motivated by the above insights, we develop a two-stage HGNN for efficient and scalable design in RIS-aided PLS systems.

III. SYSTEM MODEL AND PROBLEM FORMULATION

A. Signal Transmission

Consider a passive RIS-assisted communication system as shown in Fig. 1 where an N_T -antenna BS serves K single-antenna LUs with the assistance of an RIS equipped with L

$$R_k(\{\mathbf{w}_{k'}, \mathbf{z}_{m'}\}, \Phi) = \log_2 \left(1 + \frac{|\tilde{\mathbf{h}}_k^H(\Phi) \mathbf{w}_k|^2}{\sum_{k' \in \mathcal{K}/\{k\}} |\tilde{\mathbf{h}}_k^H(\Phi) \mathbf{w}_{k'}|^2 + \sum_{m' \in \mathcal{M}} |\tilde{\mathbf{h}}_k^H(\Phi) \mathbf{z}_{m'}|^2 + \sigma_k^2} \right) \quad (3)$$

$$R_{E,m,k}(\{\mathbf{w}_{k'}, \mathbf{z}_{m'}\}, \Phi) = \log_2 \left(1 + \frac{|\tilde{\mathbf{f}}_m^H(\Phi) \mathbf{w}_k|^2}{\sum_{k' \in \mathcal{K}/\{k\}} |\tilde{\mathbf{f}}_m^H(\Phi) \mathbf{w}_{k'}|^2 + \sum_{m' \in \mathcal{M}} |\tilde{\mathbf{f}}_m^H(\Phi) \mathbf{z}_{m'}|^2 + \sigma_{E,m}^2} \right) \quad (5)$$

reflecting elements. M single-antenna Eves intend to intercept information from the BS to LUs. For clarity, we use $k \in \mathcal{K} = \{1, 2, \dots, K\}$ to denote the k -th LU, $l \in \mathcal{L} = \{1, 2, \dots, L\}$ to denote the l -th reflecting element and $m \in \mathcal{M} = \{1, 2, \dots, M\}$ to denote the m -th Eve.

In each time slot, the transmit signal of the BS is given by

$$\mathbf{x} = \sum_{k \in \mathcal{K}} \mathbf{w}_k s_k + \sum_{m \in \mathcal{M}} \mathbf{z}_m s_0, \quad (1)$$

where s_k and $\mathbf{w}_k \in \mathbb{C}^{N_T}$ denote the information-bearing signal and the beamforming vector for the k -th LU, respectively, and $s_0 \in \mathbb{C}$ and $\mathbf{z}_m \in \mathbb{C}^{N_T}$ denote the AN signal and the AN vector for the m -th Eve, respectively. Without loss of generality, it is assumed that $\mathbb{E}\{|s_k|^2\} = 1$ and $\mathbb{E}\{|s_0|^2\} = 1$.

The received signal at the k -th LU is given by

$$y_k = \underbrace{(\mathbf{h}_{B,k}^H + \mathbf{h}_{R,k}^H \Phi \mathbf{H})}_{\triangleq \tilde{\mathbf{h}}_k^H(\Phi) \in \mathbb{C}^{N_T}} \left(\sum_{k' \in \mathcal{K}} \mathbf{w}_{k'} s_{k'} + \sum_{m' \in \mathcal{M}} \mathbf{z}_{m'} s_0 \right) + n_k, \quad (2)$$

where $\mathbf{h}_{B,k} \in \mathbb{C}^{N_T}$, $\mathbf{h}_{R,k} \in \mathbb{C}^L$, and $\mathbf{H} \in \mathbb{C}^{L \times N_T}$ respectively denote the direct CSI between the BS and the k -th LU, the CSI between the RIS and the k -th LU and the CSI between the BS and the RIS. $\Phi = \text{diag}\{e^{j\phi_1}, e^{j\phi_2}, \dots, e^{j\phi_L}\}$ denotes the phase shift matrix, where $\phi_l \in [0, 2\pi)$ denotes the phase shift of the l -th reflecting element. $n_k \sim \mathcal{CN}(0, \sigma_k^2)$ denotes the additive white Gaussian noise (AWGN) at the k -th LU. The received information rate at the k -th LU is given by (3).

Similarly, the received signal at the m -th Eve is given by

$$y_{E,m} = \underbrace{(\mathbf{f}_{B,m}^H + \mathbf{f}_{R,m}^H \Phi \mathbf{H})}_{\triangleq \tilde{\mathbf{f}}_m^H(\Phi) \in \mathbb{C}^{N_T}} \left(\sum_{k' \in \mathcal{K}} \mathbf{w}_{k'} s_{k'} + \sum_{m' \in \mathcal{M}} \mathbf{z}_{m'} s_0 \right) + n_{E,m}, \quad (4)$$

where $\mathbf{f}_{B,m} \in \mathbb{C}^{N_T}$ and $\mathbf{f}_{R,m} \in \mathbb{C}^L$ respectively denote the direct CSI from the BS and the RIS to the m -th Eve, and $n_{E,m} \sim \mathcal{CN}(0, \sigma_{E,m}^2)$ denotes the AWGN at the m -th Eve. If the m -th Eve intends to intercept the k -th LU, the information leakage data rate is expressed as (5).

The secrecy rate of the k -th LU is expressed as

$$R_{\text{Sec},k}(\{\mathbf{w}_{k'}, \mathbf{z}_{m'}\}, \Phi) = \left[R_k(\{\mathbf{w}_{k'}, \mathbf{z}_{m'}\}, \Phi) - \max_m \{R_{E,m,k}(\{\mathbf{w}_{k'}, \mathbf{z}_{m'}\}, \Phi)\} \right]^+. \quad (6)$$

B. Problem Formulation

Our goal is to jointly optimize $\{\mathbf{w}_{k'}, \mathbf{z}_{m'}, \Phi\}$ to maximize the system SEE under the constraint of the power budget denoted by P_{max} . Mathematically, this problem is formulated as

$$\max_{\{\mathbf{w}_{k'}, \mathbf{z}_{m'}, \Phi\}} \frac{\sum_{k \in \mathcal{K}} R_{\text{Sec},k}(\{\mathbf{w}_{k'}, \mathbf{z}_{m'}\}, \Phi)}{\sum_{k \in \mathcal{K}} \|\mathbf{w}_k\|^2 + \sum_{m \in \mathcal{M}} \|\mathbf{z}_m\|^2 + P_C} \quad (7a)$$

$$\text{s.t.} \quad \sum_{k \in \mathcal{K}} \|\mathbf{w}_k\|^2 + \sum_{m \in \mathcal{M}} \|\mathbf{z}_m\|^2 \leq P_{\text{max}}, \quad (7b)$$

$$\phi_l \in [0, 2\pi), l \in \mathcal{L}, \quad (7c)$$

where P_C denotes the constant power consumption.

To solve Problem (7), we leverage the learning-to-optimize approach and propose a two-stage HGNN to map CSI to $\{\mathbf{w}_{k'}, \mathbf{z}_{m'}, \Phi\}$.

IV. GRAPH REPRESENTATION

Graph representation is utilized to organize system parameters into graph-structured data and to define readout operations. The proposed model adopts a two-stage framework, where the two stages employ different heterogeneous graph representation methods to represent the considered system. Notably, compared with existing graphs designed for non-RIS and non-PLS systems [20], [21], the proposed graph captures the heterogeneity among different system entities, including the RIS, LUs, and Eves. Compared with most existing graphs representing RIS-assisted PLS systems [33], [34], the proposed graph identifies distinct RIS reflecting elements rather than regarding all elements as a single node.

Mathematically, we define a heterogeneous graph as

$$\mathcal{G} = \{\mathcal{V}_1, \dots, \mathcal{V}_N, \mathcal{E}_1, \dots, \mathcal{E}_E\}, \quad (8)$$

where N and E denote the number of node types and edge types, respectively, and \mathcal{V}_n ($n \in \{1, 2, \dots, N\}$) and \mathcal{E}_e ($e \in \{1, 2, \dots, E\}$) represent the node set of the n -th type and the edge set of the e -th type. Furthermore, the node feature matrix and edge feature matrix for all nodes in \mathcal{V}_n and all edges in \mathcal{E}_e are defined by \mathbf{X}_n and \mathbf{Y}_e , respectively.

A. Stage 1: Bipartite Graph Representation

The graph in Stage 1 is defined as

$$\mathcal{G}^{(1)} = \{\mathcal{V}_1^{(1)}, \mathcal{V}_2^{(1)}, \mathcal{V}_3^{(1)}, \mathcal{E}_1^{(1)}, \mathcal{E}_2^{(1)}\}, \quad (9)$$

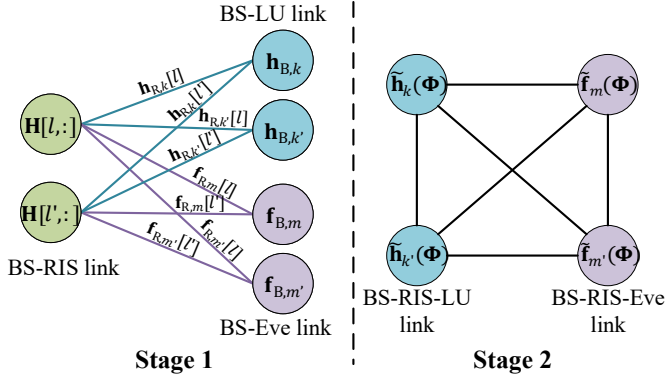


Fig. 2. Heterogeneous graph presentation and key node feature components: 1) Stage 1 constructs a bipartite graph consisting of three types of nodes corresponding to the BS-LU links, the BS-Eves links, and the BS-RIS links; 2) Stage 2 constructs a fully-connected graph consisting of two types of nodes corresponding to the BS-RIS-LU links and BS-RIS-Eve links.

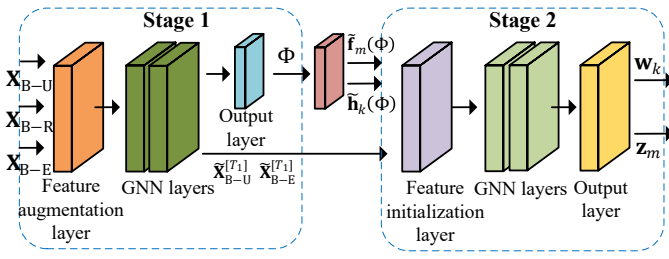


Fig. 3. Neural architecture of the two-stage HGNN: 1) Stage 1 comprises a feature augmentation layer, T_1 GNN layers, and an output layer. It maps $\{\mathbf{X}_{B-R}, \mathbf{X}_{B-U}, \mathbf{X}_{B-E}\}$ to $\{\Phi, \tilde{\mathbf{X}}_{B-U}^{[T_1]}, \tilde{\mathbf{X}}_{B-E}^{[T_1]}\}$. 2) Stage 2 consists of a feature initialization layer, T_2 GNN layers, and an output layer. It takes $\{\tilde{\mathbf{h}}_k(\Phi), \tilde{\mathbf{f}}_m(\Phi)\}$ and $\{\tilde{\mathbf{X}}_{B-U}^{[T_1]}, \tilde{\mathbf{X}}_{B-E}^{[T_1]}\}$ as inputs and outputs $\{\mathbf{w}_k, \mathbf{z}_m\}$.

which is a bipartite and undirected graph with 3 node types and 2 edge types. The structure of $\mathcal{G}^{(1)}$ is illustrated in Fig. 2. The node definition, edge definition, and readout operation are detailed as follows.

- **Node Definition:** In $\mathcal{G}^{(1)}$, there are 3 node types: 1) $|\mathcal{V}_1^{(1)}| = L$ BS-RIS link nodes, with the l -th node feature being $\mathbf{H}[l, :] \in \mathbb{C}^{N_T}$; 2) $|\mathcal{V}_2^{(1)}| = K$ BS-LU link nodes, with the k -th node feature being $\mathbf{h}_{B,k}$; 3) $|\mathcal{V}_3^{(1)}| = M$ BS-Eve link nodes, with the m -th node feature being $\mathbf{f}_{B,m}$. In summary, the node feature matrices corresponding to the three node types are defined as follows, respectively:

$$\mathbf{X}_{B-R} = \mathbf{H}' \in \mathbb{R}^{M \times 2N_T}, \quad (10)$$

$$\mathbf{X}_{B-U} = [\mathbf{h}'_{B,1}, \mathbf{h}'_{B,2}; \dots; \mathbf{h}'_{B,K}]^T \in \mathbb{R}^{K \times 2N_T}, \quad (11)$$

$$\mathbf{X}_{B-E} = [\mathbf{f}'_{B,1}, \mathbf{f}'_{B,2}; \dots; \mathbf{f}'_{B,M}]^T \in \mathbb{R}^{L \times 2N_T}, \quad (12)$$

where

$$\mathbf{H}' = \text{Concat}(\text{real}(\mathbf{H}), \text{imag}(\mathbf{H})) \in \mathbb{R}^{M \times 2N_T}, \quad (13)$$

$$\mathbf{h}'_{B,i} = \text{Concat}(\text{real}(\mathbf{h}_{B,i}), \text{imag}(\mathbf{h}_{B,i})) \in \mathbb{R}^{2N_T}, \quad (14)$$

$$\mathbf{f}'_{B,i} = \text{Concat}(\text{real}(\mathbf{f}_{B,i}), \text{imag}(\mathbf{f}_{B,i})) \in \mathbb{R}^{2N_T}. \quad (15)$$

- **Edge Definition:** In $\mathcal{G}^{(1)}$, there are 2 undirected edge

types: 1) $|\mathcal{E}_1^{(1)}| = L \times K$ edges, each connecting one BS-RIS link node and one BS-LU link node, with the $\langle l, k \rangle$ -th edge feature being $\mathbf{h}_{R,k}[l]$; 2) $|\mathcal{E}_2^{(1)}| = L \times M$ edges, each connecting one BS-RIS link node and one BS-Eve link node, with the $\langle l, m \rangle$ -th edge feature being $\mathbf{f}_{R,m}[l]$.

- **Readout Operation:** The HGNN in Stage 1 updates the features of $(L + K + M)$ nodes. The updated feature of L BS-RIS link nodes are readout as Φ , which is fed into both Stage 2 (cf. (42)) and the loss function (cf. (58)). The updated features of each BS-LU link node and each BS-Eve link node are used as augmented features (cf. (42) and (43)) for beamforming learning and AN learning, respectively, in Stage 2.

B. Stage 2: Fully-Connected Graph Representation

The graph in Stage 2 is defined as

$$\mathcal{G}^{(2)} = \{\mathcal{V}_1^{(2)}, \mathcal{V}_2^{(2)}, \mathcal{E}_1^{(2)}, \mathcal{E}_2^{(2)}, \mathcal{E}_3^{(2)}\}, \quad (16)$$

which is a fully-connected and undirected graph. The structure of $\mathcal{G}^{(2)}$ is illustrated in Fig. 2. The node definition, edge definition, and readout operation are detailed as follows.

- **Node Definition:** In $\mathcal{G}^{(2)}$, there are 2 node types: 1) $|\mathcal{V}_1^{(2)}| = K$ BS-RIS-LU link nodes, where the k -th node feature (cf. (42)) consists of $\tilde{\mathbf{h}}_k(\Phi)$ and the augmented feature of the k -th BS-LU node yielded by Stage 1; 2) $|\mathcal{V}_2^{(2)}| = M$ BS-RIS-Eve link nodes, where the m -th node feature consists of $\tilde{\mathbf{f}}_m(\Phi)$ and the augmented feature (cf. (43)) of the m -th BS-Eve node yielded by Stage 1. Here, Φ is derived from Stage 1.
- **Edge Definition:** In $\mathcal{G}^{(2)}$, there are three types of edges which connect two BS-RIS-LU link nodes, one BS-RIS-LU link node and one BS-RIS-Eve link node, and two BS-RIS-Eve link nodes, respectively. But all edges are non-feature.
- **Readout Operation:** The HGNN in Stage 2 updates the features of $(K + M)$ nodes. The updated features of the k -th BS-RIS-LU link node and the m -th BS-RIS-Eve link node are used to readout relevant parameters for the k -th beamforming vector and m -th AN vector, respectively.

V. TWO-STAGE HGNN

The overall computational process of the two-stage HGNN is illustrated in Fig. 3, and the models of the two stages incorporate some similar operations based on the meta-paths [35]. For clarity, we first define the common operations and then introduce the architectures of the models in the two stages, respectively.

A. Common Operations

1) **Subgraph Extraction Operations:** To flexibly extract the intra-graph features, two types of subgraph extraction operations are defined over a given graph \mathcal{G} .

- **Unidirectional bipartite graph extraction operation:**

$$\tilde{\mathcal{G}}_{D-BG} = \psi_{\text{Uni}}(\mathcal{V}_n, \mathcal{V}_{n'}), \quad (17)$$

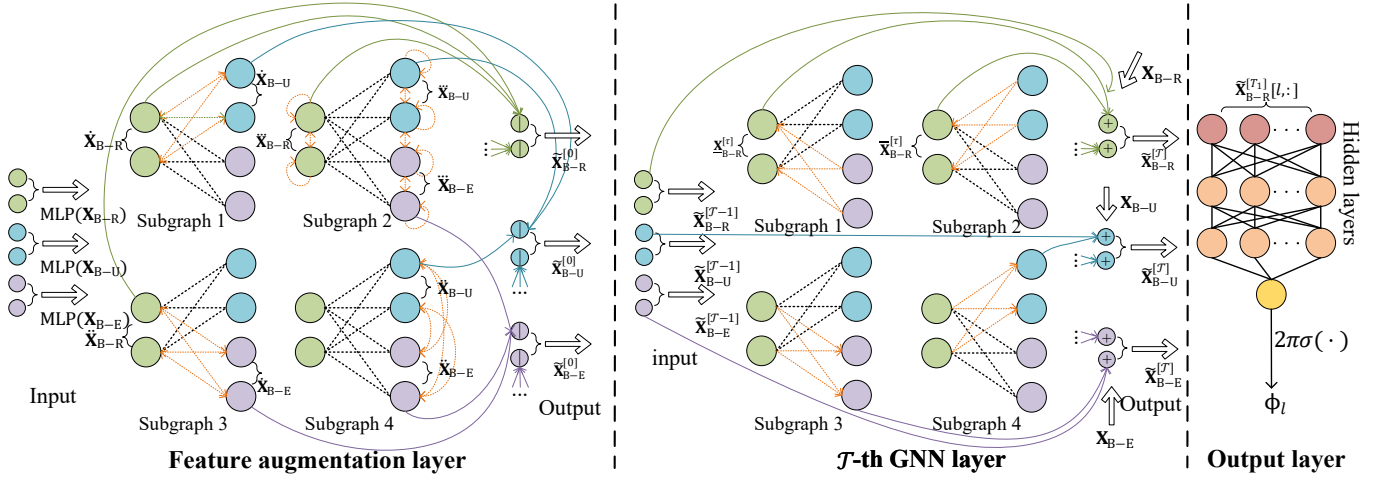


Fig. 4. Illustration of key processes in Stage 1: 1) The feature augmentation layer maps $\{\mathbf{X}_{B-R}, \mathbf{X}_{B-U}, \mathbf{X}_{B-E}\}$ to $\{\tilde{\mathbf{X}}_{B-R}^{[0]}, \tilde{\mathbf{X}}_{B-U}^{[0]}, \tilde{\mathbf{X}}_{B-E}^{[0]}\}$ via GAT on four subgraphs. 2) The τ -th GNN layer maps $\{\tilde{\mathbf{X}}_{B-R}^{[\tau-1]}, \tilde{\mathbf{X}}_{B-U}^{[\tau-1]}, \tilde{\mathbf{X}}_{B-E}^{[\tau-1]}\}$ combined with the residual terms $\{\tilde{\mathbf{X}}_{B-R}^{[\tau-1]}, \tilde{\mathbf{X}}_{B-U}^{[\tau-1]}, \tilde{\mathbf{X}}_{B-E}^{[\tau-1]}, \mathbf{X}_{B-R}, \mathbf{X}_{B-U}, \mathbf{X}_{B-E}\}$ to $\{\tilde{\mathbf{X}}_{B-R}^{[\tau]}, \tilde{\mathbf{X}}_{B-U}^{[\tau]}, \tilde{\mathbf{X}}_{B-E}^{[\tau]}\}$ via GAT on four subgraphs. 3) The output layer maps $\{\tilde{\mathbf{X}}_{B-R}^{[\tau]}[l, :]\}$ to $\{\phi_l\}$ using an MLP.

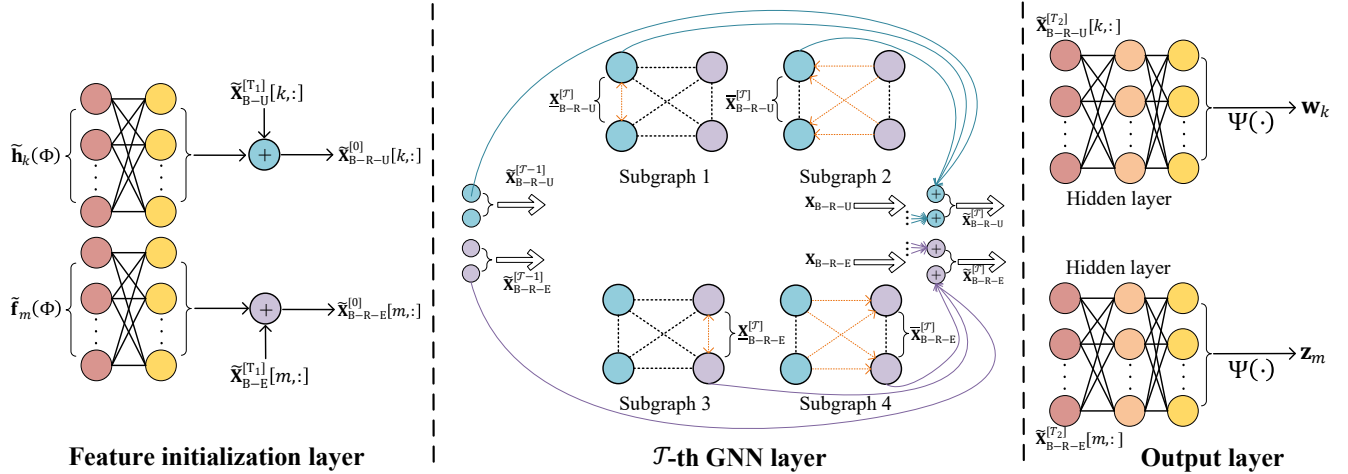


Fig. 5. Illustration of key processes in Stage 2: 1) The feature initialization layer employs two separate MLPs to map $\{\tilde{\mathbf{h}}_k, \tilde{\mathbf{f}}_m\}$ to intermediate values, respectively. These values are then summed with $\{\tilde{\mathbf{X}}_{B-U}^{[\tau]}[k, :], \tilde{\mathbf{X}}_{B-E}^{[\tau]}[m, :]\}$ to obtain $\{\tilde{\mathbf{X}}_{B-R-U}^{[0]}[k, :], \tilde{\mathbf{X}}_{B-R-E}^{[0]}[m, :]\}$. 2) The τ -th GNN layer maps $\{\tilde{\mathbf{X}}_{B-R-U}^{[\tau-1]}, \tilde{\mathbf{X}}_{B-R-E}^{[\tau-1]}\}$ combined with the residual terms $\{\tilde{\mathbf{X}}_{B-R-U}^{[\tau-1]}, \tilde{\mathbf{X}}_{B-R-E}^{[\tau-1]}, \mathbf{X}_{B-R-U}, \mathbf{X}_{B-R-E}\}$ to $\{\tilde{\mathbf{X}}_{B-R-U}^{[\tau]}, \tilde{\mathbf{X}}_{B-R-E}^{[\tau]}\}$ via GAT on four subgraphs. 3) The output layer uses two separate MLPs to map $\{\tilde{\mathbf{X}}_{B-R-U}^{[\tau]}[k, :], \tilde{\mathbf{X}}_{B-R-E}^{[\tau]}[m, :]\}$ to $\{\mathbf{w}_k, \mathbf{z}_m\}$, respectively.

where \mathcal{V}_n and $\mathcal{V}_{n'}$ denote two node sets of distinct types, and $\tilde{\mathcal{G}}_{D-BG}$ is a subgraph of \mathcal{G} that forms a directed bipartite graph. The extracted subgraph $\tilde{\mathcal{G}}_{D-BG}$ consists of two node sets, i.e., \mathcal{V}_n and $\mathcal{V}_{n'}$, along with directed¹ edges from each node in \mathcal{V}_n to each node in $\mathcal{V}_{n'}$. The nodes and edges in $\tilde{\mathcal{G}}_{D-BG}$ have consistent features with those in \mathcal{G} .

- Bidirectional bipartite graph extraction operation:

$$\tilde{\mathcal{G}}_{UD-BG} = \psi_{Bi}(\mathcal{V}_n, \mathcal{V}_{n'}), \quad (18)$$

where $\tilde{\mathcal{G}}_{UD-BG}$ is a subgraph of \mathcal{G} that forms an

¹Even for an undirected \mathcal{G} , a directed subgraph can be constructed, since an undirected edge can be treated as bidirectional edges sharing the identical features.

undirected bipartite graph. The only difference between $\tilde{\mathcal{G}}_{UD-BG}$ and $\tilde{\mathcal{G}}_{D-BG}$ is that the edges in $\tilde{\mathcal{G}}_{UD-BG}$ are undirected.

- 2) *Fully-Connected Graph Construction Operation*: To exploit the similarity among nodes with the same type, the fully-connected graph construction operation is defined by

$$\tilde{\mathcal{G}}_{UD-FC} = \psi_{FC}(\mathcal{V}_n), \quad (19)$$

where $\tilde{\mathcal{G}}_{UD-FC}$ is a fully-connected and undirected graph consisting of nodes in \mathcal{V}_n with undirected and feature-free edges connecting these nodes. The nodes inherit the features from their original \mathcal{G} .

- 3) *Graph Attention Operators*: To distinguish the interactions between nodes, two types of graph attention operators are

defined, which adapt to different graph-structured features. The output dimensions of the both operators are uniformly set to $D \times B$, where D and B denote the number of attention heads and the projection dimension of a single head, respectively.

- Edge-based graph attention operator:

$$\{\mathbf{X}_n\}_{n \in \{1,2,\dots,N'\}} := v_{\text{EAtt}}(\mathcal{G}, \{\mathbf{X}_n\}), \quad (20)$$

where $N' \leq N$ denotes the number of target node types.

- Edge-free graph attention operator:

$$\{\mathbf{X}_n\}_{n \in \{1,2,\dots,N'\}} := v_{\text{Att}}(\mathcal{G}, \{\mathbf{X}_n\}). \quad (21)$$

The detailed processes of the two attention operators are detailed in the Appendix A and B. Notably, the learnable parameters and output dimensions of both operators are associated with the input graph.

B. Stage 1: Phase Shift Matrix Learning over $\mathcal{G}^{(1)}$

In Stage 1, we utilize an HGNN to learn the phase shift matrix over $\mathcal{G}^{(1)}$ through three sequential modules: 1) the feature augmentation layer; 2) T_1 GNN layers; and 3) the phase shift output layer. The detailed computational process of the HGNN is illustrated in Fig. 4.

1) *Feature Augmentation Layer*: This module is designed to enhance the initial input features, yielding the inputs for the first GNN layer, which are defined by $\tilde{\mathbf{X}}_{\text{B-U}}^{[0]}$, $\tilde{\mathbf{X}}_{\text{B-E}}^{[0]}$, and $\tilde{\mathbf{X}}_{\text{B-R}}^{[0]}$.

We first apply a single-layer MLP to enhance the initial dimension, which expands the feature space and improves the model's expressive capacity before subsequent feature processing.

$$\mathbf{X}'_{\text{B-R}}[l, :] = \text{LeakyReLU}(\mathbf{W}_1 \mathbf{X}_{\text{B-R}}[l, :]), \quad (22)$$

$$\mathbf{X}'_{\text{B-U}}[k, :] = \text{LeakyReLU}(\mathbf{W}_1 \mathbf{X}_{\text{B-U}}[k, :]), \quad (23)$$

$$\mathbf{X}'_{\text{B-E}}[m, :] = \text{LeakyReLU}(\mathbf{W}_1 \mathbf{X}_{\text{B-E}}[m, :]), \quad (24)$$

where \mathbf{W}_1 is a learnable weight matrix.

We employ graph attention operations to obtain

$$\{\dot{\mathbf{X}}_{\text{B-R}}, \dot{\mathbf{X}}_{\text{B-U}}\} = v_{\text{EAtt}}\left(\psi_{\text{Bi}}\left(\mathcal{V}_1^{(1)}, \mathcal{V}_2^{(1)}\right), \mathbf{X}'_{\text{B-R}}, \mathbf{X}'_{\text{B-U}}\right), \quad (25)$$

$$\{\ddot{\mathbf{X}}_{\text{B-R}}, \ddot{\mathbf{X}}_{\text{B-E}}\} = v_{\text{EAtt}}\left(\psi_{\text{Bi}}\left(\mathcal{V}_1^{(1)}, \mathcal{V}_3^{(1)}\right), \mathbf{X}'_{\text{B-R}}, \mathbf{X}'_{\text{B-E}}\right)', \quad (26)$$

$$\{\ddot{\mathbf{X}}_{\text{B-U}}, \ddot{\mathbf{X}}_{\text{B-E}}\} = v_{\text{Att}}\left(\psi_{\text{FC}}\left(\mathcal{V}_2^{(1)}, \mathcal{V}_3^{(1)}\right), \mathbf{X}'_{\text{B-U}}, \mathbf{X}'_{\text{B-E}}\right), \quad (27)$$

$$\{\ddot{\mathbf{X}}_{\text{B-R}}, \ddot{\mathbf{X}}_{\text{B-U}}, \ddot{\mathbf{X}}_{\text{B-E}}\} = v_{\text{Att}}\left(\psi_{\text{FC}}\left(\mathcal{V}_1^{(1)}\right) \cup \psi_{\text{FC}}\left(\mathcal{V}_2^{(1)}\right) \cup \psi_{\text{FC}}\left(\mathcal{V}_3^{(1)}\right), \mathbf{X}'_{\text{B-R}}, \mathbf{X}'_{\text{B-U}}, \mathbf{X}'_{\text{B-E}}\right), \quad (28)$$

and then, construct

$$\tilde{\mathbf{X}}_{\text{B-U}}^{[0]} = \text{Concat}\left(\dot{\mathbf{X}}_{\text{B-U}}, \ddot{\mathbf{X}}_{\text{B-U}}, \ddot{\mathbf{X}}_{\text{B-E}}\right), \quad (29)$$

$$\tilde{\mathbf{X}}_{\text{B-E}}^{[0]} = \text{Concat}\left(\dot{\mathbf{X}}_{\text{B-E}}, \ddot{\mathbf{X}}_{\text{B-E}}, \ddot{\mathbf{X}}_{\text{B-E}}\right), \quad (30)$$

$$\tilde{\mathbf{X}}_{\text{B-R}}^{[0]} = \text{Concat}\left(\dot{\mathbf{X}}_{\text{B-R}}, \ddot{\mathbf{X}}_{\text{B-R}}, \ddot{\mathbf{X}}_{\text{B-R}}\right). \quad (31)$$

2) *GNN Layers*: T_1 GNN layers update the node feature matrix for each node type using graph attention operators and residual connections.

At the τ -th layer, the node feature matrices are first computed as

$$\tilde{\mathbf{X}}_{\text{B-U}}^{[\tau]} = v_{\text{EAtt}}\left(\psi_{\text{Uni}}\left(\mathcal{V}_1^{(1)}, \mathcal{V}_2^{(1)}\right), \tilde{\mathbf{X}}_{\text{B-R}}^{[\tau-1]}, \tilde{\mathbf{X}}_{\text{B-U}}^{[\tau-1]}\right), \quad (32)$$

$$\tilde{\mathbf{X}}_{\text{B-E}}^{[\tau]} = v_{\text{EAtt}}\left(\psi_{\text{Uni}}\left(\mathcal{V}_1^{(1)}, \mathcal{V}_3^{(1)}\right), \tilde{\mathbf{X}}_{\text{B-R}}^{[\tau-1]}, \tilde{\mathbf{X}}_{\text{B-E}}^{[\tau-1]}\right), \quad (33)$$

$$\tilde{\mathbf{X}}_{\text{B-R}}^{[\tau]} = \overline{\mathbf{X}}_{\text{B-R}}^{[\tau]} + \underline{\mathbf{X}}_{\text{B-R}}^{[\tau]}, \quad (34)$$

where

$$\overline{\mathbf{X}}_{\text{B-R}}^{[\tau]} = v_{\text{EAtt}}\left(\psi_{\text{Uni}}\left(\mathcal{V}_2^{(1)}, \mathcal{V}_1^{(1)}\right), \tilde{\mathbf{X}}_{\text{B-U}}^{[\tau-1]}, \tilde{\mathbf{X}}_{\text{B-R}}^{[\tau-1]}\right), \quad (35)$$

$$\underline{\mathbf{X}}_{\text{B-R}}^{[\tau]} = v_{\text{EAtt}}\left(\psi_{\text{Uni}}\left(\mathcal{V}_3^{(1)}, \mathcal{V}_1^{(1)}\right), \tilde{\mathbf{X}}_{\text{B-E}}^{[\tau-1]}, \tilde{\mathbf{X}}_{\text{B-R}}^{[\tau-1]}\right). \quad (36)$$

Then, these node feature matrices undergo residual connections [36] to mitigate the gradient vanishing problem caused by layer stacking:

$$\tilde{\mathbf{X}}_{\text{B-U}}^{[\tau]} := \tilde{\mathbf{X}}_{\text{B-U}}^{[\tau]} + P(\mathbf{X}_{\text{B-U}}) + P\left(\tilde{\mathbf{X}}_{\text{B-U}}^{[\tau-1]}\right), \quad (37)$$

$$\tilde{\mathbf{X}}_{\text{B-E}}^{[\tau]} := \tilde{\mathbf{X}}_{\text{B-E}}^{[\tau]} + P(\mathbf{X}_{\text{B-E}}) + P\left(\tilde{\mathbf{X}}_{\text{B-E}}^{[\tau-1]}\right), \quad (38)$$

$$\tilde{\mathbf{X}}_{\text{B-R}}^{[\tau]} := \tilde{\mathbf{X}}_{\text{B-R}}^{[\tau]} + P(\mathbf{X}_{\text{B-R}}) + P\left(\tilde{\mathbf{X}}_{\text{B-R}}^{[\tau-1]}\right), \quad (39)$$

where $P(\cdot)$ is the zero-padding operation, aiming to align the dimensions of the matrices in a lightweight manner.

3) *Phase Shift Output Layer*: For the l -th reflecting element, its phase shift is obtained by

$$\phi_l = 2\pi \times \text{sigmoid}\left(\mathbf{c}_1 \text{LeakyReLU}\left(\mathbf{W}_2 \text{LeakyReLU}\left(\mathbf{W}_3 \tilde{\mathbf{X}}_{\text{B-R}}^{[T_1]}[l, :]\right)\right)\right), \quad (40)$$

where \mathbf{c}_1 , \mathbf{W}_2 , and \mathbf{W}_3 are learnable parameters. Then, the phase shift matrix is output as

$$\Phi = \text{diag}\left\{[e^{j\phi_1}, e^{j\phi_2}, \dots, e^{j\phi_L}]\right\}. \quad (41)$$

C. Stage 2: Beamforming and AN Learning over $\mathcal{G}^{(2)}$

In Stage 2, we utilize an HGNN to learn the beamforming vectors and AN vectors over $\mathcal{G}^{(2)}$ through three sequential modules: 1) the feature initialization layer; 2) T_2 GNN layers; and 3) the beamforming and AN output layer. The detailed computational process of the HGNN is illustrated in Fig. 5.

1) *Feature Initialization Layer*: With the obtained Φ , the effective CSI for the k -th LU and the m -th Eve are derived as $\tilde{\mathbf{h}}_k(\Phi)$ and $\tilde{\mathbf{f}}_m(\Phi)$. The node feature matrices for the two node types in $\mathcal{G}^{(2)}$ are initialized by fusing the effective CSI and the outputs of Stage 1, which are given respectively by

$$\tilde{\mathbf{X}}_{\text{B-R-U}}^{[0]}[k, :] = \text{LeakyReLU}\left(\mathbf{W}_4 \tilde{\mathbf{h}}_k(\Phi)\right) + \tilde{\mathbf{X}}_{\text{B-U}}^{[T_1]}[k, :], \quad (42)$$

$$\tilde{\mathbf{X}}_{\text{B-R-E}}^{[0]}[m, :] = \text{LeakyReLU}\left(\mathbf{W}_5 \tilde{\mathbf{f}}_m(\Phi)\right) + \tilde{\mathbf{X}}_{\text{B-E}}^{[T_1]}[m, :], \quad (43)$$

where \mathbf{W}_4 and \mathbf{W}_5 are learnable weight matrices to align the dimensions of the matrices.

2) T_2 GNN Layers: T_2 GNN layers update the node feature matrix for each node type using graph attention operators and residual connections.

At the τ -th layer, the node feature matrices are first computed as

$$\tilde{\mathbf{X}}_{\text{B-R-U}}^{[\tau]} = \overline{\mathbf{X}}_{\text{B-R-U}}^{[\tau]} + \underline{\mathbf{X}}_{\text{B-R-U}}^{[\tau]}, \quad (44)$$

$$\tilde{\mathbf{X}}_{\text{B-R-E}}^{[\tau]} = \overline{\mathbf{X}}_{\text{B-R-E}}^{[\tau]} + \underline{\mathbf{X}}_{\text{B-R-E}}^{[\tau]}, \quad (45)$$

where

$$\overline{\mathbf{X}}_{\text{B-R-U}}^{[\tau]} = v_{\text{Att}} \left(\psi_{\text{Uni}} \left(\mathcal{V}_1^{(2)}, \mathcal{V}_2^{(2)} \right), \tilde{\mathbf{X}}_{\text{B-R-U}}^{[\tau-1]}, \tilde{\mathbf{X}}_{\text{B-R-E}}^{[\tau-1]} \right), \quad (46)$$

$$\overline{\mathbf{X}}_{\text{B-R-E}}^{[\tau]} = v_{\text{Att}} \left(\psi_{\text{Uni}} \left(\mathcal{V}_2^{(2)}, \mathcal{V}_1^{(2)} \right), \tilde{\mathbf{X}}_{\text{B-R-E}}^{[\tau-1]}, \tilde{\mathbf{X}}_{\text{R-R-U}}^{[\tau-1]} \right), \quad (47)$$

$$\underline{\mathbf{X}}_{\text{B-R-U}}^{[\tau]} = v_{\text{Att}} \left(\psi_{\text{FC}} \left(\mathcal{V}_1^{(2)} \right), \tilde{\mathbf{X}}_{\text{B-R-U}}^{[\tau-1]} \right), \quad (48)$$

$$\underline{\mathbf{X}}_{\text{B-U-E}}^{[\tau]} = v_{\text{Att}} \left(\psi_{\text{FC}} \left(\mathcal{V}_2^{(2)} \right), \tilde{\mathbf{X}}_{\text{B-R-E}}^{[\tau-1]} \right). \quad (49)$$

The residual connections are introduced to alleviate the gradient vanishing problem, and the final output of each layer is

$$\tilde{\mathbf{X}}_{\text{B-R-U}}^{[\tau]} := \tilde{\mathbf{X}}_{\text{B-R-U}}^{[\tau]} + P(\mathbf{X}_{\text{B-R-U}}) + P\left(\tilde{\mathbf{X}}_{\text{B-R-U}}^{[\tau-1]}\right), \quad (50)$$

$$\tilde{\mathbf{X}}_{\text{B-R-E}}^{[\tau]} := \tilde{\mathbf{X}}_{\text{B-R-E}}^{[\tau]} + P(\mathbf{X}_{\text{B-R-E}}) + P\left(\tilde{\mathbf{X}}_{\text{B-R-E}}^{[\tau-1]}\right), \quad (51)$$

where

$$\mathbf{X}_{\text{B-R-U}} \triangleq \left[\tilde{\mathbf{h}}_1(\Phi), \tilde{\mathbf{h}}_2(\Phi); \dots; \tilde{\mathbf{h}}_K(\Phi) \right], \quad (52)$$

$$\mathbf{X}_{\text{B-R-E}} \triangleq \left[\tilde{\mathbf{f}}_1(\Phi), \tilde{\mathbf{f}}_2(\Phi); \dots; \tilde{\mathbf{f}}_M(\Phi) \right]. \quad (53)$$

3) *Beamforming and AN Output Layer*: We consider two output methods, i.e., beam-direct and model-based.

The beam-direct output enables $(K+L)$ nodes to share two fully-connected layers and one activation function to directly map the final node embeddings $\tilde{\mathbf{X}}_{\text{B-R-U}}^{[T_2]}$ and $\tilde{\mathbf{X}}_{\text{B-R-E}}^{[T_2]}$ to the unconstrained beamforming vector and AN vector:

$$\tilde{\mathbf{w}}_k = f_2 \left(\mathbf{W}_6 \text{LeakyReLU} \left(\mathbf{W}_7 \tilde{\mathbf{X}}_{\text{B-R-U}}^{[T_2]} [k, :] + \boldsymbol{\eta}_1 \right) + \boldsymbol{\eta}_2 \right), \quad (54)$$

$$\tilde{\mathbf{z}}_m = f_2 \left(\mathbf{W}_8 \text{LeakyReLU} \left(\mathbf{W}_9 \tilde{\mathbf{X}}_{\text{B-R-E}}^{[T_2]} [m, :] + \boldsymbol{\eta}_3 \right) + \boldsymbol{\eta}_4 \right), \quad (55)$$

where $\mathbf{W}_6, \mathbf{W}_7, \mathbf{W}_8, \mathbf{W}_9, \boldsymbol{\eta}_1, \boldsymbol{\eta}_2, \boldsymbol{\eta}_3,$ and $\boldsymbol{\eta}_4$ are learnable weights, and $f_2(\cdot) : \mathbb{R}^{2N_T} \rightarrow \mathbb{C}^{N_T}$ is a dimension reshaping function. Then, $\{\tilde{\mathbf{w}}_k\}$ and $\{\tilde{\mathbf{z}}_m\}$ undergo the following operation to meet the total power budget constraint:

$$\Psi(\mathbf{v}_i) = \sqrt{\frac{P_{\max}}{\max \left(P_{\max}, \sum_{i' \in \mathcal{K} \cup \mathcal{M}} \|\mathbf{v}_{i'}\|^2 \right)}} \mathbf{v}_i, \quad (56)$$

where $\mathbf{v}_n \in \{\mathbf{w}_k, \mathbf{z}_m\}_{k \in \mathcal{K}, m \in \mathcal{M}}$.

The model-based output utilizes the hybrid zero forcing (ZF) and maximum ratio transmission (MRT) method [37], which defines (α_k, p_k) and (β_m, p_m) in the Appendix C, where α_k and β_m represent the direction-related parameters, and p_k and p_m represents the power-related parameters. The model-based output employs two fully-connected layers along with one activation function to yield (α_k, p_k) for the k -th

LU and (β_m, p_m) for the m -th Eve. Specifically, to meet the constraints, α_k and β_m are activated via the Sigmoid function, while p_k and p_m undergo the ReLU function along with

$$\tilde{\Psi}(p_i) = \sqrt{\frac{P_{\max}}{\max \left(P_{\max}, \sum_{i' \in \mathcal{K} \cup \mathcal{M}} p_{i'} \right)}} p_i, \quad (57)$$

where $p_i \in \{p_k, p_m\}_{k \in \mathcal{K}, m \in \mathcal{M}}$.

D. Loss Function

We adopt unsupervised learning to train the proposed model, and the loss function is given by

$$\mathcal{L} = - \frac{\sum_{k \in \mathcal{K}} \tilde{R}_{\text{Sec},k}(\{\mathbf{w}_{k'}, \mathbf{z}_{m'}\}, \Phi)}{\sum_{k \in \mathcal{K}} \|\mathbf{w}_k\|^2 + \sum_{m \in \mathcal{M}} \|\mathbf{z}_m\|^2 + P_C}, \quad (58)$$

where $\tilde{R}_{\text{Sec},k}(\{\mathbf{w}_{k'}, \mathbf{z}_{m'}\}, \Phi)$ is given by

$$\begin{aligned} \tilde{R}_{\text{Sec},k}(\{\mathbf{w}_{k'}, \mathbf{z}_{l'}\}, \Phi) = \\ R_k(\{\mathbf{w}_{k'}, \mathbf{z}_{m'}\}, \Phi) - \gamma \max_m \{R_{\text{E},m,k}(\{\mathbf{w}_{k'}, \mathbf{z}_{m'}\}, \Phi)\}, \end{aligned} \quad (59)$$

where γ is a hyperparameter, which is usually set to 0.1.

E. Scalability Analysis

Notably, all learnable parameters in the proposed two-stage HGNN are independent of the number of reflecting elements L , LUs K , and Eves M . This property stems from the permutation equivariance inherent in the graph representations and graph operations employed in the model.

1) *Permutation-Equivariant Graph Representation*: The graph in Stage 1 incorporates three types of nodes corresponding to reflecting elements, LUs, and Eves, where both LU nodes and Eve nodes are connected to reflecting element nodes. The graph in Stage 2 is fully-connected, which consists of two types of nodes corresponding to LUs and Eves, where the features of both node types involve the phase shift matrix. The graphs utilized in both stages satisfy permutation equivariance, i.e., permuting the input order of the same node type does not alter the model's output or optimization results. Such a property renders the model inherently adaptable to dynamic numbers of reflecting elements, LUs, and Eves. In particular, this can be achieved simply by adding or removing corresponding nodes in the graph, while the core message-passing mechanism remains unchanged and no retraining is necessitated.

2) *Permutation-Equivariant Graph Operation*: The key operator employed in both stages relies on the multi-head attention mechanism from GAT. Such a mechanism is inherently permutation-equivariant. That is, arbitrary permutations of the input node set, including the rearrangement of node indices and their associated features, yield identical permutations of the output node representations, without altering the model's core computational logic or the relative relationships among the learned node embeddings. When new nodes are added to the graph, the model automatically integrates them into the message-passing procedure by computing attention weights between the newly introduced nodes and existing ones according to their feature similarities, without any modification

TABLE II
THE STRUCTURE OF THE TWO-STAGE HGNN.

Stage	Type	IFs	HNs	OFs	AHs
1	FIL	$2N_T$	640	32	5
	GL	1	480	×	64
		2	640	×	64
	OL	640	320, 128	1	×
2	FAL	$2N_T$	×	640	×
	GL	1	640	×	128
		2	1280	×	256
	OL	2560	640	$2N_T$	×

GL/FAL/FIL/OL: GNN layer/Feature augmentation layer/Feature initialization layer/Output layer.

IFs/OFs/HNs/AHs: Input features/Output features/Number of neurons in hidden layer/Number of attention heads.

TABLE III
TRAINING AND TEST SET CONFIGURATIONS.

Training set		Test set	
(L_{Tr}, K_{Tr}, M_{Tr})		(L_{Te}, K_{Te}, M_{Te})	
(8, 3, 4)		(8, 3, 4)	
		(8, 2, 4)	
		(8, 4, 4)	
		(7, 3, 4)	
		(9, 3, 4)	
		(8, 3, 3)	
		(8, 3, 5)	
#Sample	9.6×10^5	#Sample	1000 per set

to the pre-trained model parameters. Similarly, when nodes are removed, the model simply excludes the corresponding nodes from the message aggregation and attention computation steps, while the underlying message-passing mechanism remains unchanged.

VI. NUMERICAL RESULTS

This section evaluates the proposed model. The structures of the proposed model are displayed in Table II.

A. Experimental Setting

1) *Simulation Scenario*: The BS is deployed at (0, 0) m, while the RIS is placed at (10, 0) m close to the BS to mitigate cascaded fading. The LUs are randomly distributed within a circular area centered at (50, 50) m with a radius of 10 m, and the Eves are randomly distributed within a circular area centered at (25, 25) m with a radius of 10 m. Notably, Eves are closer to the BS than LUs. The transmit antennas at BS are set as $N_T = 8$.

2) *Channel Model*: The path loss of direct link (including $\mathbf{h}_{B,k}$ and $\mathbf{f}_{B,m}$) is modeled as $\sqrt{\rho d^{-\alpha}}$ where d and ρ denote the corresponding Euclidean distance and the path loss per meter distance, respectively, and α denotes the fading exponent. The small-scale fading is modeled as Rayleigh fading.

The RIS-related CSI contains one LoS path and a large number of NLoS paths. Specifically, the CSI between the RIS

TABLE IV
SIMULATION PARAMETERS.

Notation	Values
BS location	(0, 0)
RIS location	(10, 0)
LU location	center (50, 50) radius 10
Eve location	center (25, 25) radius 10
Number of antennas	$N_T = 8$
Central frequency	$f_c = 1.8$ GHz
Constant power	$P_C = 0.5$ W
Antenna separation	$\Delta = \lambda/2$
Wavelength	$\lambda = c/f_c$
Rician factor	$\beta = 3$ dB
Fading exponent	$\alpha = 2.8$
Power budget	$P_{\max} = 30$ dBm
Path loss per meter	$\rho = -20$ dB
Noise power	$\sigma^2 = -80$ dBm

and a receiver (either an LU or an Eve), or between the BS and the RIS, is modeled using Rician fading, which is given by

$$\mathbf{h} = \sqrt{\rho d^{-\alpha}} \left(\sqrt{\frac{\beta}{1+\beta}} \mathbf{h}^{\text{LoS}}(\phi) + \sqrt{\frac{1}{\beta+1}} \mathbf{h}^{\text{NL}} \right), \quad (60)$$

$$\mathbf{H} = \sqrt{\rho d^{-\alpha}} \left(\sqrt{\frac{\beta}{1+\beta}} \mathbf{H}^{\text{LoS}}(\phi) + \sqrt{\frac{1}{\beta+1}} \mathbf{H}^{\text{NL}} \right), \quad (61)$$

where β denotes the Rician factor, and the entries of $\mathbf{h}^{\text{NL}}/\mathbf{H}^{\text{NL}}$ are independently drawn from the complex Gaussian distribution with zero mean and unit variance, i.e., $\mathcal{CN}(0, 1)$. The LoS components are expressed by the responses of the ULA. For an N -element ULA, the response is given by

$$\mathbf{a}_N(\phi) = \left[1, e^{-j\frac{2\pi}{\lambda}\Delta \sin(\phi)}, \dots, e^{-j\frac{2\pi}{\lambda}(N-1)\Delta \sin(\phi)} \right]^T, \quad (62)$$

where Δ and λ denote antenna separation and wavelength, respectively, and ϕ denotes the angle of departure (AoD) or angle of arrival (AoA) of a signal. Then, \mathbf{h}^{LoS} and \mathbf{H}^{LoS} are respectively given by

$$\mathbf{h}^{\text{LoS}} = \mathbf{a}_L(\phi_{\text{AoD}}), \quad (63)$$

$$\mathbf{H}^{\text{LoS}} = \mathbf{a}_L(\phi_{\text{AoA}}) \mathbf{a}_{N_T}^H(\phi_{\text{AoD}}). \quad (64)$$

All default parameters are summarized in Table IV.

3) *Dataset and Metric*: We prepare one training set with 9.6×10^5 samples and seven test sets with 1000 samples each. The training set adopts the setting of $(L_{Tr}, K_{Tr}, M_{Tr}) = (8, 3, 4)$, while the configurations of the test sets are provided in Table III.

All samples in both the training set and test sets are generated independently according to the channel model. Moreover, for each test sample, we employ the BCD method to obtain its optimal SEE as the label. During the test, we use the ratio of the SEE yielded by the DL model to the SEE label as the evaluation metric.

TABLE V
PERFORMANCE COMPARISON.

N_T	Training Setting (L_{Tr}, K_{Tr}, M_{Tr})	Test Setting (L_{Te}, K_{Te}, M_{Te})	Baselines			Two-stage HGNN		Note
			MLP	CO-GNN	BHGNN	Beam-direct	Model-based	
8	(8, 3, 4)	(8, 3, 4)	23.57%	61.61%	34.87%	90.76%	96.60%	
		(8, 2, 4)	28.31%	50.28%	49.59%	82.01%	96.80%	Scale to
		(8, 4, 4)	–	25.35%	2.01%	45.20%	96.99%	L
		(7, 3, 4)	–	–	23.98%	89.54%	96.46%	Scale to
		(9, 3, 4)	–	–	25.26%	89.73%	96.43%	K
		(8, 3, 3)	25.72%	63.03%	37.30%	91.56%	97.27%	Scale to
		(8, 3, 5)	–	61.06%	34.14%	79.39%	95.93%	M
Inference time			0.73 ms	0.99 ms	2.3 ms	11.53 ms	11.64 ms	82.74 s by CVXopt

4) *Implementation Details*: The learning rate is initialized as 1×10^{-4} . The adaptive moment estimation is adopted as the optimizer during the training phase. The batch size is set to 256 for 100 epochs of training, and the learnable weights with the best performance are used as the training result. Our implementation is developed using Python 3.11.5 with PyTorch 2.1.0 on a computer with Intel(R) Core(TM) Ultra 9 275HX CPU and one NVIDIA GeForce RTX 5070 Ti Laptop GPU (12 GB of memory).

5) *Baselines*: The baselines employed to evaluate the effectiveness of the proposed two-stage HGNN are listed as follows:

- MLP: A basic feed-forward neural network with a three-branch output architecture.
- CO-GNN: A GNN model with one RIS node and multiple LU nodes, which adopts a custom message-passing mechanism integrating mean-pooling, max-pooling, and MLP-based node feature update, similar to [34].
- BHGNN: A GNN model with multiple RIS nodes, multiple LU nodes, and edge feature integration, which adopts a custom message-passing mechanism integrating sum-pooling, MLP-based node feature update, and iterative optimization update, similar to [32].

B. Effectiveness

Table V compares the proposed two-stage HGNN with the baselines. For identical training and test settings, i.e., $(L_{Tr}, K_{Tr}, M_{Tr}) = (L_{Te}, K_{Te}, M_{Te})$, the proposed two-stage HGNN achieves a higher SEE using both the beam-direct and model-based output methods, where the model-based one can attain near-optimal performance. However, the existing baselines fail to yield satisfactory performance. Especially, the MLP achieves a performance near 20%, highlighting the necessity of developing task-suitable neural architectures. The two-stage HGNN, COGNN and BHGNN are scalable with respect to the number of reflecting elements and Eves. As observed, only the two-stage HGNN with the model-based output method can maintain a good performance. In contrast, the two-stage HGNN with the beam-direct output method suffers from a notable performance degradation when encountering a larger L or M . Furthermore, the baselines

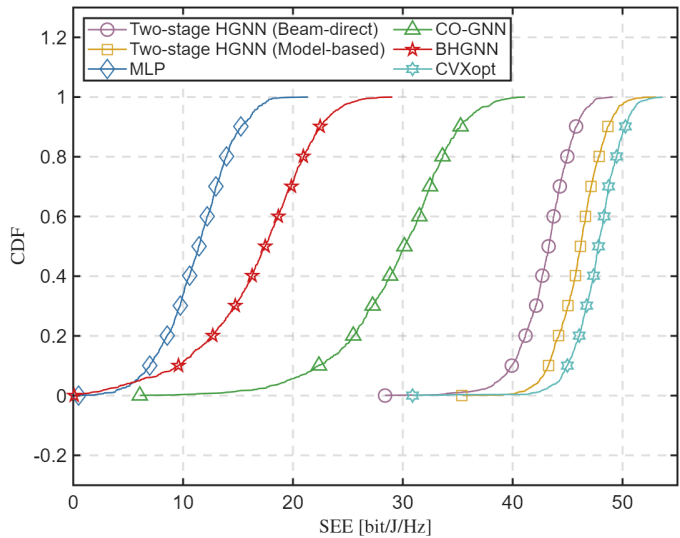


Fig. 6. CDF of SEE for DL-based and CVXopt-based approaches.

exhibit even poorer performance. The two-stage HGNN and BHGNN are scalable with respect to the number of LUs K . In this scenario, both the beam-direct and model-based output methods maintain limited performance loss, whereas BHGNN does not scale well. Moreover, the two-stage HGNN requires longer inference time for the transmit design than the baselines, since it involves more sophisticated designs in both framework and architecture. Nevertheless, it still maintains millisecond-level efficiency, which is considerably faster than the CVXopt-based approach. In summary, the two-stage HGNN yields near-optimal performance, with a notable performance improvement over the baselines. Moreover, the two-stage HGNN, especially with the model-based output method, scales well with respect to the number of reflecting elements, LUs, and Eves, demonstrating its adaptability to dynamic wireless environments.

Fig. 6 plots the cumulative distribution function (CDF) of the achievable SEE for the proposed model and baselines as well as the CVXopt-based approach over 1000 test samples, with $(L_{Tr}, K_{Tr}, M_{Tr}) = (L_{Te}, K_{Te}, M_{Te}) = (8, 3, 4)$. Compared with the baselines, the two-stage HGNN yields more

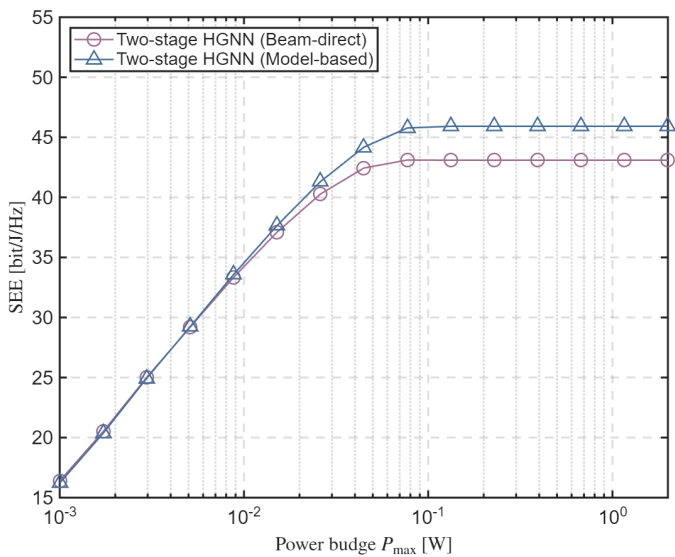


Fig. 7. SEE versus power budget by the two-stage HGNN trained with $P_{\max} = 1$ W.

stable SEE performance and significantly reduces the probability of low SEE. Particularly, the model-based method allows the two-stage HGNN to achieve performance comparable to that of the CVXopt-based approach for all test samples, while requiring much less inference time.

Fig. 7 illustrates the achievable SEE by the proposed two-stage HGNN trained with $P_{\max} = 30$ dBm over the power budget range $[0, 33]$ dBm. Results for both the beam-direct and model-based output methods are provided. It can be observed that the SEE first increases and then remains unchanged with the power budget, which is consistent with the theoretical results [38]. That is, the two-stage HGNN can learn the key characteristics of the SEE function, enabling it to adapt to various power budgets. Such a capability is derived by the parameter-free scaling operation (56) and (57). Moreover, the model-based output method behaves comparably to the beam-direct one at low power budgets, while achieving superior performance at high power budgets.

Fig. 8 illustrates the scalability of the two-stage HGNN with respect to the number of LUs K or Eves M over a range $[2, 7]$. During the training phase, K and M are set to 3 and 4, respectively, and the model-based output method is employed. It can be observed that the two-stage HGNN accurately captures the trend that the achievable SEE increases with K , which is consistent with the simulation results in [6]. Moreover, as M increases, the SEE achieved by the two-stage HGNN degrades, since it becomes increasingly challenging to prevent information leakage, which is consistent with the simulation results in [39]. Notably, such scalability is obtained without retraining, making it highly crucial for adapting to the dynamics of wireless networks.

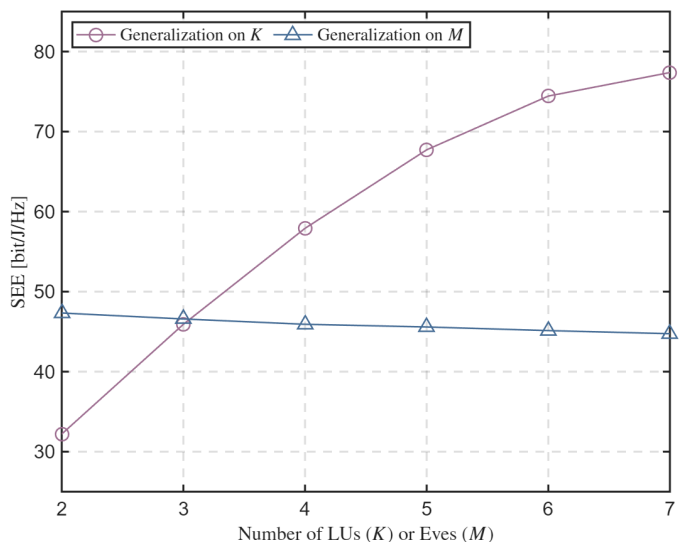


Fig. 8. Generalization performance of the two-stage GNN with the model-based output method with $K_{\text{Tr}} = 3$ and $M_{\text{Tr}} = 4$.

C. Ablation Experiment

Table VI presents the ablation study² to validate the effectiveness of three key components, i.e., the residual connection, the two-stage framework, and the model-based output method. As observed, all components contribute to the performance improvement. For clarity, we report the average gain compared with the model without the three components. Specifically, the residual connection and the two-stage framework improve the achievable SEE by 1.54% and 19.07%, respectively, and their combination yields a 27.67% performance gain. This result demonstrates that the basic GNN model for RIS-assisted systems can be effectively built upon the two-stage framework with residual connections. The model-based output method contributes to an average gain of 43.56%, which mainly benefits from its stable performance when scaling to different system configurations. Thus, it is essential to integrate theoretical results into the neural network architecture.

VII. CONCLUSION

This paper focused on developing a GNN-based learning-to-optimize approach for RIS-aided PLS systems. We proposed to jointly exploit the multi-stage framework and the heterogeneous graph representation to tackle the deeply coupled optimization variables and inherent system heterogeneity. Specifically, a two-stage HGNN is developed to maximize the system SEE. The two-stage HGNN follows a stage-wise graph modeling strategy: the first stage constructs a bipartite graph to learn the optimal RIS phase shift matrix, while the second stage employs a fully-connected heterogeneous graph to generate beamforming and AN vectors. Multi-head attention mechanisms and residual connections are integrated into both stages to enhance feature learning and model stability. Trained in an unsupervised manner, the two-stage HGNN avoids the

²The ablation study on HGNN is intractable, since the considered system deviates significantly from the homogeneous graph representation.

TABLE VI
ABLATION EXPERIMENT WITH $(L_r, K_{Tr}, M_{Tr}) = (8, 3, 4)$.

Res	Two-Stage	Model-based	(L_{Te}, K_{Te}, M_{Te})						Average Gain	
			$(8, 3, 4)$	$(8, 2, 4)$	$(8, 4, 4)$	$(7, 3, 4)$	$(9, 3, 4)$	$(8, 3, 3)$		$(8, 3, 5)$
×	×	×	58.70%	63.99%	36.00%	45.54%	51.20%	58.93%	57.14%	–
✓	×	×	60.35%	55.87%	34.69%	54.80%	56.73%	60.77%	59.10%	1.54%
×	✓	×	87.12%	65.54%	38.04%	86.07%	86.21%	88.09%	53.97%	19.07%
✓	✓	×	90.76%	82.01%	42.20%	89.54%	89.73%	91.56%	79.39%	27.67%
✓	✓	✓	96.60%	96.80%	96.99%	96.46%	96.43%	97.27%	95.93%	43.56%

$$\alpha_d^{(i,j)} = \frac{\exp\left(\mathbf{a}_d^T \text{LeakyReLU}\left(\mathbf{W}_d^{(S)} \mathbf{x}_i + \mathbf{W}_d^{(N)} \mathbf{x}_j + \mathbf{W}_d^{(E)} \mathbf{y}_{i,j}\right)\right)}{\sum_{i' \in \mathcal{N}(i)} \exp\left(\mathbf{a}_d^T \text{LeakyReLU}\left(\mathbf{W}_d^{(S)} \mathbf{x}_i + \mathbf{W}_d^{(N)} \mathbf{x}_{i'} + \mathbf{W}_d^{(E)} \mathbf{y}_{i,i'}\right)\right)} \quad (65)$$

dependence on large labeled datasets and reduces the computational burden. Its scalable structure enables flexible adaptation to dynamic numbers of RIS elements, LUs, and Eves. Numerical results confirmed the superiority of the proposed HGNN over state-of-the-art GNNs in RIS-aided PLS scenarios. Compared with CVXopt-based algorithms, it drastically reduces the inference time while limiting the performance degradation to below 4%. Furthermore, its scalability under various system configurations is verified.

APPENDIX

A. Edge-Based Graph Attention Operator

Given a graph \mathcal{G} and the corresponding node feature matrices $\{\mathbf{X}_n\}$, the edge-based graph attention operator is detailed as follows to update the node feature matrices.

For clarity, we define the \mathbf{x}_i (derived from $\{\mathbf{X}_n\}$) by the node feature of the i -th node, $\mathcal{N}(i)$ by the neighboring source node set of the i -th node, and $\mathbf{y}_{i,i'}$ by the directed edge feature from the i' -th ($i' \in \mathcal{N}(i)$) node to the i -th node, which keeps unchanged.

The i -th target node assigns an attention coefficient associated with the d -th ($d \in \{1, 2, \dots, D\}$) head to its j -th ($j \in \mathcal{N}(i)$) source node, which is calculated by (65), where \mathbf{a}_d denotes the learnable attention weight vector, and $\mathbf{W}_d^{(S)}$, $\mathbf{W}_d^{(N)}$, and $\mathbf{W}_d^{(E)}$ denote the learnable projection matrices for target node, source node, and edge features, respectively.

Then, the i -th node aggregates the node features of itself and its neighboring target nodes based on the d -th attention head to obtain

$$\beta_d^{(i)} = \mathbf{W}_d^{(S)} \mathbf{x}_i + \sum_{i' \in \mathcal{N}(i)} \alpha_d^{(i,i')} \left(\mathbf{W}_d^{(N)} \mathbf{x}_{i'} + \mathbf{W}_d^{(E)} \mathbf{y}_{i,i'} \right), \quad (66)$$

By concatenating the D aggregated features, the feature of the i -th node is updated to $\tilde{\mathbf{x}}_i$, which is given by

$$\tilde{\mathbf{x}}_i = \text{Concat} \left(\left\{ \beta_d^{(i)} \right\} \right). \quad (67)$$

B. Edge-Free Graph Attention Operator

Similarly, the edge-free graph attention operator updates node features of a given graph \mathcal{G} without involving the edge features.

We reuse the symbols defined for simplicity. The d -th attention coefficient assigned by the i -th target node to the j -th source node is given by

$$\alpha_d^{(i,j)} = \frac{\exp\left(\mathbf{a}_d^T \text{LeakyReLU}\left(\mathbf{W}_d^{(S)} \mathbf{x}_i + \mathbf{W}_d^{(N)} \mathbf{x}_j\right)\right)}{\sum_{i' \in \mathcal{N}(i)} \exp\left(\mathbf{a}_d^T \text{LeakyReLU}\left(\mathbf{W}_d^{(S)} \mathbf{x}_i + \mathbf{W}_d^{(N)} \mathbf{x}_{i'}\right)\right)}. \quad (68)$$

Then, the node feature of the i -th node is updated by

$$\tilde{\mathbf{x}}_i = \text{Concat} \left(\left\{ \sum_{i' \in \mathcal{N}(i)} \alpha_d^{(i,i')} \mathbf{W}_d^{(N)} \mathbf{x}_{i'} \right\} \right). \quad (69)$$

C. Hybrid ZF and MRT method

We represent \mathbf{w}_k and \mathbf{z}_m as

$$\mathbf{w}_k = \sqrt{p_k} \bar{\mathbf{w}}_k (\alpha_k), \quad \|\bar{\mathbf{w}}_k (\alpha_k)\| = 1, \quad (70)$$

$$\mathbf{z}_m = \sqrt{p_m} \bar{\mathbf{z}}_m (\beta_m), \quad \|\bar{\mathbf{z}}_m (\beta_m)\| = 1. \quad (71)$$

For \mathbf{w}_k , the hybrid ZF and MRT scheme is adopted to design its direction, which is given by

$$\bar{\mathbf{w}}_k (\alpha_k) = \frac{\alpha_k \frac{\mathbf{v}_k}{\|\mathbf{v}_k\|} + (1 - \alpha_k) \frac{\tilde{\mathbf{h}}_k(\Phi)}{\|\tilde{\mathbf{h}}_k(\Phi)\|}}{\left\| \alpha_k \frac{\mathbf{v}_k}{\|\mathbf{v}_k\|} + (1 - \alpha_k) \frac{\tilde{\mathbf{h}}_k(\Phi)}{\|\tilde{\mathbf{h}}_k(\Phi)\|} \right\|}, \quad (72)$$

where $\alpha_k \in [0, 1]$ is a learnable parameter, and \mathbf{v}_k is the k -th column of

$$\mathbf{V} \triangleq \mathbf{G}^H (\mathbf{G} \mathbf{G}^H)^{-1}, \quad (73)$$

where $\mathbf{G} \triangleq [\tilde{\mathbf{h}}_1(\Phi), \tilde{\mathbf{h}}_2(\Phi), \dots, \tilde{\mathbf{h}}_K(\Phi)]$.

For \mathbf{z}_m , its direction is given by

$$\bar{\mathbf{z}}_m (\beta_m) = \frac{\beta_m \frac{\mathbf{v}_{\text{Eve},m}}{\|\mathbf{v}_{\text{Eve},m}\|} + (1 - \beta_m) \frac{\tilde{\mathbf{f}}_m(\Phi)}{\|\tilde{\mathbf{f}}_m(\Phi)\|}}{\left\| \beta_m \frac{\mathbf{v}_{\text{Eve},m}}{\|\mathbf{v}_{\text{Eve},m}\|} + (1 - \beta_m) \frac{\tilde{\mathbf{f}}_m(\Phi)}{\|\tilde{\mathbf{f}}_m(\Phi)\|} \right\|}, \quad (74)$$

where $\beta_m \in [0, 1]$ is a learnable parameter, and $\mathbf{v}_{\text{Eve},m}$ is the $(k+1)$ -th column of

$$\mathbf{V}_{\text{Eve},m} \triangleq \mathbf{G}_{\text{Eve},m}^H (\mathbf{G}_{\text{Eve},m} \mathbf{G}_{\text{Eve},m}^H)^{-1}, \quad (75)$$

where $\mathbf{G}_{\text{Eve},m} \triangleq [\tilde{\mathbf{h}}_1(\Phi), \tilde{\mathbf{h}}_2(\Phi), \dots, \tilde{\mathbf{h}}_K(\Phi), \tilde{\mathbf{f}}_m(\Phi)]$.

REFERENCES

- [1] Q. Wu and R. Zhang, "Towards smart and reconfigurable environment: Intelligent reflecting surface aided wireless network," *IEEE Commun. Mag.*, vol. 58, no. 1, pp. 106–112, Jan. 2020.
- [2] M. A. ElMossallamy, H. Zhang, L. Song, K. G. Seddik, Z. Han, and G. Y. Li, "Reconfigurable intelligent surfaces for wireless communications: Principles, challenges, and opportunities," *IEEE Trans. Cognit. Commun. Networking*, vol. 6, no. 3, pp. 990–1002, Sept. 2020.
- [3] Y. Liu, X. Liu, X. Mu, T. Hou, J. Xu, M. Di Renzo, and N. Al-Dhahir, "Reconfigurable intelligent surfaces: Principles and opportunities," *IEEE Commun. Surv. Tutorials*, vol. 23, no. 3, pp. 1546–1577, 2021.
- [4] S. Hong, C. Pan, H. Ren, K. Wang, and A. Nallanathan, "Artificial-noise-aided secure MIMO wireless communications via intelligent reflecting surface," *IEEE Trans. Commun.*, vol. 68, no. 12, pp. 7851–7866, Dec. 2020.
- [5] H. Amiriara, F. Ashtiani, M. Mirmohseni, and M. Nasiri-Kenari, "IRS-user association in IRS-aided MISO wireless networks: Convex optimization and machine learning approaches," *IEEE Trans. Veh. Technol.*, vol. 72, no. 11, pp. 14305–14316, Nov. 2023.
- [6] Y. Lu, "Secrecy energy efficiency in RIS-assisted networks," *IEEE Trans. Technol.*, vol. 72, no. 9, pp. 12419–12424, Sept. 2023.
- [7] H. Guo, Y.-C. Liang, J. Chen, and E. G. Larsson, "Weighted sum-rate maximization for reconfigurable intelligent surface aided wireless networks," *IEEE Trans. Wireless Commun.*, vol. 19, no. 5, pp. 3064–3076, May 2020.
- [8] C. Pan, G. Zhou, K. Zhi, S. Hong, T. Wu, Y. Pan, H. Ren, M. D. Renzo, A. Lee Swindlehurst, R. Zhang, and A. Y. Zhang, "An overview of signal processing techniques for RIS/IRS-aided wireless systems," *IEEE J. Sel. Top. Signal Process.*, vol. 16, no. 5, pp. 883–917, Aug. 2022.
- [9] C. Huang, R. Mo, and C. Yuen, "Reconfigurable intelligent surface assisted multiuser MISO systems exploiting deep reinforcement learning," *IEEE J. Sel. Areas Commun.*, vol. 38, no. 8, pp. 1839–1850, Aug. 2020.
- [10] R. Zhang, K. Xiong, Y. Lu, P. Fan, D. W. K. Ng, and K. B. Letaief, "Energy efficiency maximization in RIS-assisted SWIPT networks with RSMA: A PPO-based approach," *IEEE J. Sel. Areas Commun.*, vol. 41, no. 5, pp. 1413–1430, May 2023.
- [11] A. S. Abdalla and V. Marojevic, "Enhancing secrecy energy efficiency in RIS-aided aerial mobile edge computing networks: A deep reinforcement learning approach," in *Proc. ICC*, 2025, pp. 6585–6590.
- [12] H. Sun, X. Chen, Q. Shi, M. Hong, X. Fu, and N. D. Sidiropoulos, "Learning to optimize: Training deep neural networks for interference management," *IEEE Trans. Signal Process.*, vol. 66, no. 20, pp. 5438–5453, Oct. 2018.
- [13] P. Saikia, K. Singh, S. K. Singh, W.-J. Huang, C.-P. Li, and S. Biswas, "Beamforming design in vehicular communication systems with multiple reconfigurable intelligent surfaces: A deep learning approach," *IEEE Access*, vol. 11, pp. 100832–100844, 2023.
- [14] J. Gao, C. Zhong, X. Chen, H. Lin, and Z. Zhang, "Unsupervised learning for passive beamforming," *IEEE Commun. Lett.*, vol. 24, no. 5, pp. 1052–1056, May 2020.
- [15] Y. Ma, X. Zhou, X. Li, L. Liang, and S. Jin, "Unsupervised learning-based joint resource allocation and beamforming design for RIS-assisted MISO-OFDMA systems," *IEEE Trans. Cognit. Commun. Networking*, vol. 12, pp. 2251–2264, 2026.
- [16] H. Zhang, Q. Jia, M. Li, J. Wang, and Y. Song, "Passive Beamforming Design of IRS-Assisted MIMO Systems Based on Deep Learning," *Sensors*, vol. 23, no. 16, p. 7164, Aug. 2023.
- [17] Y. Lu, S. Zhang, C. Liu, R. Zhang, B. Ai, D. Niyato, W. Ni, X. Wang, and A. Jamalipour, "Agentic graph neural networks for wireless communications and networking toward edge general intelligence: A survey," *IEEE Commun. Surv. Tutorials*, vol. 28, pp. 4519–4554, 2026.
- [18] Y. Lu, Y. Li, R. Zhang, W. Chen, B. Ai, and D. Niyato, "Graph neural networks for wireless networks: Graph representation, architecture and evaluation," *IEEE Wireless Commun.*, vol. 32, no. 1, pp. 150–156, Feb. 2025.
- [19] Y. Shen, J. Zhang, S. H. Song, and K. B. Letaief, "Graph neural networks for wireless communications: From theory to practice," *IEEE Trans. Wireless Commun.*, vol. 22, no. 5, pp. 3554–3569, May 2023.
- [20] Y. Li, Y. Lu, B. Ai, O. A. Dobre, Z. Ding, and D. Niyato, "GNN-based beamforming for sum-rate maximization in MU-MISO networks," *IEEE Trans. Wireless Commun.*, vol. 23, no. 8, pp. 9251–9264, Aug. 2024.
- [21] C. He, Y. Lu, B. Ai, O. A. Dobre, Z. Ding, and D. Niyato, "ICGNN: Graph neural network enabled scalable beamforming for MISO interference channels," *IEEE Trans. Mob. Comput.*, vol. 24, no. 10, pp. 10778–10791, Oct. 2025.
- [22] Z. Song, Y. Lu, X. Chen, B. Ai, Z. Zhong, and D. Niyato, "A deep learning framework for physical-layer secure beamforming," *IEEE Trans. Veh. Technol.*, vol. 73, no. 12, pp. 19844–19849, Dec. 2024.
- [23] J. Yang, J. Xu, Y. Zhang, H. Zheng, and T. Zhang, "Graph attention network-based precoding for reconfigurable intelligent surfaces aided wireless communication systems," *IEEE Trans. Veh. Technol.*, vol. 73, no. 6, pp. 9098–9102, June 2024.
- [24] C. He, Y. Lu, Y. Xu, C.-Y. Chi, B. Ai, and A. Nallanathan, "RIS-assisted downlink pinching-antenna systems: GNN-enabled optimization approaches," *arXiv preprint arXiv:2511.20305*, Nov. 2025. [Online]. Available: <https://arxiv.org/abs/2511.20305>
- [25] T.-J. Yeh, W.-C. Tsai, C.-W. Chen, and A.-Y. Wu, "Enhanced-GNN with angular csi for beamforming design in IRS-assisted mmWave communication systems," *IEEE Commun. Lett.*, vol. 28, no. 4, pp. 827–831, April 2024.
- [26] H. Tang, J. Zhang, Z. Zhao, H. Wu, H. Sun, and P. Jiao, "Joint optimization based on two-phase GNN in RIS- and DF-assisted MISO systems with fine-grained rate demands," *IEEE Trans. Wireless Commun.*, vol. 24, no. 12, pp. 9989–10002, Dec. 2025.
- [27] B. Yin, J. Schampheleer, W. Joseph, and M. Deruyck, "Graph neural network-based energy-efficient optimization for RIS-assisted wireless networks," *IEEE Trans. Wireless Commun.*, vol. 25, pp. 664–680, 2026.
- [28] M. Liu, C. Huang, A. Alhammadi, M. Di Renzo, M. Debbah, and C. Yuen, "Beamforming design and association scheme for multi-RIS multi-user mmWave systems through graph neural networks," *IEEE Trans. Wireless Commun.*, vol. 24, no. 9, pp. 7940–7954, Sept. 2025.
- [29] T. N. Kipf and M. Welling, "Semi-supervised classification with graph convolutional networks," in *Proc. ICLR*, Apr. 2017.
- [30] P. Veličković, G. Cucurull, A. Casanova, A. Romero, P. Liò, and Y. Bengio, "Graph attention networks," in *Proc. ICLR*, Apr. 2018.
- [31] Q.-S. Nguyen, X.-T. Dang, and O.-S. Shin, "Optimization of RIS-assisted cell-free massive MIMO systems with heterogeneous graph neural networks under imperfect channel estimation," *IEEE Trans. Veh. Technol.*, pp. 1–16, 2025.
- [32] H. A. Le, T. Van Chien, and W. Choi, "Graph neural network-based active and passive beamforming for distributed STAR-RIS-assisted multi-user MISO systems," *IEEE Trans. Commun.*, vol. 73, no. 10, pp. 9299–9312, Oct. 2025.
- [33] J. Zhang, H. Tang, P. Jiao, H. Wu, Z. Zhao, and R. Li, "Secrecy rate optimization based on GNN for RIS-assisted ISAC system," *IEEE Internet Things J.*, pp. 1–1, 2026.
- [34] L. Liang, Z. Tian, H. Huang, X. Li, Z. Yin, D. Zhang, N. Zhang, and W. Zhai, "Heterogeneous secure transmissions in IRS-assisted NOMA communications: CO-GNN approach," *IEEE Internet Things J.*, vol. 12, no. 16, pp. 34113–34125, Aug. 2025.
- [35] X. Wang, H. Ji, C. Shi, B. Wang, Y. Ye, P. Cui, and P. S. Yu, "Heterogeneous graph attention network," in *Proc. World Wide Web Conf. (WWW)*, May 2019, pp. 2022–2032.
- [36] X. Zheng, Z. Liu, J. Liang, Y. Wu, Y. Chen, and Q. Zhang, "Residual learning and multi-path feature fusion-based channel estimation for millimeter-wave massive MIMO system," *Entropy*, vol. 24, no. 2, p. 292, Feb. 2022.
- [37] R. Zhang, Y. Lu, W. Chen, B. Ai, and Z. Ding, "Model-based GNN enabled energy-efficient beamforming for ultra-dense wireless networks," *IEEE Trans. Wireless Commun.*, vol. 24, no. 4, pp. 3333–3345, 2025.
- [38] Y. Li, M. Sheng, C. Yang, and X. Wang, "Energy efficiency and spectral efficiency tradeoff in interference-limited wireless networks," *IEEE Commun. Lett.*, vol. 17, no. 10, pp. 1924–1927, Oct. 2013.
- [39] W. Hao, J. Li, G. Sun, C. Huang, M. Zeng, O. A. Dobre, and C. Yuen, "Robust security energy efficiency optimization for RIS-aided cell-free networks with multiple eavesdroppers," *IEEE Trans. Commun.*, vol. 72, no. 12, pp. 7401–7416, Dec. 2024.